

1 **Distal and proximal controls on the silicon stable isotope signature of North Atlantic Deep**

2 **Water**

3
4 Gregory F. de Souza^{a,1,*}, Richard D. Slater^a, Mathis P. Hain^b, Mark A. Brzezinski^c, and Jorge L.
5 Sarmiento^a

6
7 ^aProgram in Atmospheric and Oceanic Sciences, Princeton University, Princeton, New Jersey 08544,
8 USA

9 ^bNational Oceanography Centre, University of Southampton, Southampton SO14 3ZH, UK

10 ^cMarine Science Institute, University of California, Santa Barbara, CA 93106, USA

11
12
13 * to whom correspondence should be addressed: ETH Zurich, Institute of Geochemistry and
14 Petrology, NW C81.3, Clausiusstrasse 25, 8092 Zurich, Switzerland; Tel: +41 44 632 6983; E-mail:
15 desouza@erdw.ethz.ch

16
17 accepted for publication in *Earth and Planetary Science Letters*

18 18th October 2015

19 <http://dx.doi.org/10.1016/j.epsl.2015.10.025>

20
21
22
23
24 © 2015. This manuscript is made available under the CC-BY-NC-ND 4.0 license

25 <http://creativecommons.org/licenses/by-nc-nd/4.0/>



¹ Present address: ETH Zurich, Institute of Geochemistry and Petrology, 8092 Zurich, Switzerland

28 **Abstract**

29 It has been suggested that the uniquely high $\delta^{30}\text{Si}$ signature of North Atlantic Deep Water (NADW)
30 results from the contribution of isotopically fractionated silicic acid by mode and intermediate waters
31 that are formed in the Southern Ocean and transported to the North Atlantic within the upper limb of
32 the meridional overturning circulation (MOC). Here, we test this hypothesis in a suite of ocean general
33 circulation models (OGCMs) with widely varying MOCs and related pathways of nutrient supply to
34 the upper ocean. Despite their differing MOC pathways, all models reproduce the observation of a
35 high $\delta^{30}\text{Si}$ signature in NADW, as well showing a major or dominant (46–62%) contribution from
36 Southern Ocean mode/intermediate waters to its Si inventory. These models thus confirm that the $\delta^{30}\text{Si}$
37 signature of NADW does indeed owe its existence primarily to the large-scale transport of a distal
38 fractionation signal created in the surface Southern Ocean. However, we also find that more proximal
39 fractionation of Si upwelled to the surface within the Atlantic Ocean must also play some role,
40 contributing 20–46% of the deep Atlantic $\delta^{30}\text{Si}$ gradient. Finally, the model suite reveals
41 compensatory effects in the mechanisms contributing to the high $\delta^{30}\text{Si}$ signature of NADW, whereby
42 less export of high- $\delta^{30}\text{Si}$ mode/intermediate waters to the North Atlantic is compensated by production
43 of a high- $\delta^{30}\text{Si}$ signal during transport to the NADW formation region. This trade-off decouples the
44 $\delta^{30}\text{Si}$ signature of NADW from the pathways of deep water upwelling associated with the MOC. Thus,
45 whilst our study affirms the importance of cross-equatorial transport of Southern Ocean-sourced Si in
46 producing the unique $\delta^{30}\text{Si}$ signature of NADW, it also shows that the presence of a deep Atlantic
47 $\delta^{30}\text{Si}$ gradient does not uniquely constrain the pathways by which deep waters are returned to the
48 upper ocean.

49

50 **Keywords:** biogeochemical cycles, silicon isotopes, meridional overturning circulation

51

52 **1. Introduction**

53 *1.1. Marine Si cycling and the $\delta^{30}\text{Si}$ distribution*

54 The cycling of nutrients in the sea is determined by a complex set of interactions between biota in
55 the surface ocean and the physical circulation across a range of spatial and temporal scales. At the
56 global scale, the export of nutrients to the abyss in biogenic particles is balanced by the supply of
57 dissolved nutrients via the upwelling of nutrient-rich deep waters in the MOC (Broecker and Peng,
58 1982; Sarmiento et al., 2007). At the scale of the thermocline, nutrient distributions are determined by
59 how the location and timing of biological nutrient drawdown at the surface interacts with the
60 subduction of water masses and their gyre- to basin-scale circulation (Sarmiento et al., 2004; Palter et
61 al., 2005; Karleskind et al., 2011). These distributions in turn determine the magnitude, biogeography
62 and distribution of low-latitude primary productivity (Marinov et al., 2006; Palter et al., 2010, 2011).
63 The ocean interior distributions of nutrients thus both influence and are influenced by biological
64 productivity, and bear the imprint of the interaction between productivity and the ocean's three-
65 dimensional circulation, allowing them to be used to infer the physical and biological interactions that
66 determine marine nutrient cycling. This study takes such an approach in order to trace the influence of
67 physical-biological interactions on the large-scale transports associated with the marine cycle of
68 silicon (Si).

69 Of the ocean's photosynthesising primary producers, diatoms are the most important group for the
70 export of organic carbon from the surface ocean (e.g. Buesseler, 1998). As a result, they play a key
71 role in the biological pump, a mechanism by which the ocean modulates atmospheric pCO_2 (Hain et
72 al., 2014a). Whilst their opaline cell wall, or frustule, provides diatoms protection from predators
73 (Smetacek, 1999) and is less energy-intensive to produce than an organic cell wall (Raven, 1983), it
74 also makes them vitally dependent on the presence of Si dissolved in seawater. The boom-bust
75 behaviour of diatom populations that leads to their importance for carbon export also means that
76 diatoms are very efficient exporters of Si to depth (Brzezinski et al., 2003), such that they are the main
77 driver of marine Si cycling (Tréguer and De La Rocha, 2013). Diatom uptake of Si discriminates
78 between its isotopes, with lighter Si isotopes being preferentially incorporated into the frustule (De La
79 Rocha et al., 1997; Sutton et al., 2013), leaving the residual Si in seawater enriched in heavier Si

80 isotopes. Diatom Si uptake at the ocean's surface thus produces a signal of biological cycling in the
81 stable isotope composition of seawater Si (expressed in the standard delta notation as $\delta^{30}\text{Si}$), which can
82 be used as a tracer of the marine Si cycle (e.g. Cardinal et al., 2005; Reynolds et al., 2006; Beucher et
83 al., 2008; de Souza et al., 2012a; Grasse et al., 2013). For instance, diatom uptake in the surface
84 Southern Ocean produces elevated $\delta^{30}\text{Si}$ in the deep winter mixed layers from which the Southern
85 Ocean mode/intermediate water masses Subantarctic Mode Water (SAMW) and Antarctic
86 Intermediate Water (AAIW) are ventilated (Fripiat et al., 2011). This isotopic signal is transported into
87 the subtropical interior by the spreading of these water masses from their formation regions (de Souza
88 et al., 2012b).

89 The clearest large-scale signal in the marine $\delta^{30}\text{Si}$ distribution is the $\delta^{30}\text{Si}$ gradient in the deep
90 Atlantic Ocean (Fig. 1a; de Souza et al., 2012a; Brzezinski and Jones, 2015), with a systematic trend
91 from high $\delta^{30}\text{Si}$ values in deep waters of the Si-poor North Atlantic, influenced by NADW, to lower
92 values towards the Si-richer south, influenced by Antarctic Bottom Water (AABW). This coherent
93 gradient is related to the quasi-conservative mixing of Si between these two water masses (Broecker et
94 al., 1991), as reflected by the systematics (Fig. 1a) and water-column distribution (Fig. 1b) of $\delta^{30}\text{Si}$ in
95 the Atlantic, both of which indicate water-mass control on the $\delta^{30}\text{Si}$ distribution. de Souza et al.
96 (2012a) suggested that the high $\delta^{30}\text{Si}$ value of NADW ultimately results from the creation of a high-
97 $\delta^{30}\text{Si}$ signal by diatom Si uptake in the surface Southern Ocean, a signal that is transported to the
98 North Atlantic by SAMW/AAIW in the upper limb of the MOC. This mechanism has since been
99 invoked to explain the isotope distributions of other biogeochemically-cycled elements, such as
100 cadmium (e.g. Abouchami et al., 2014).

101 Such a Southern-Ocean-focused mechanism is consistent with burgeoning evidence that the
102 dominant MOC pathway by which dense and nutrient-rich deep waters are brought to the surface is the
103 wind-driven upwelling in the Southern Ocean (Toggweiler and Samuels, 1993; Sarmiento et al., 2004;
104 Lumpkin and Speer, 2007; Marshall and Speer, 2012; Morrison et al., 2015), contrary to the canonical
105 view of upwelling through the low-latitude thermocline (Robinson and Stommel, 1959; Broecker and
106 Peng, 1982). However, some recent observationally-based estimates of global overturning indicate a
107 significant role of low-latitude upwelling in closing the MOC (Talley et al., 2003; Talley, 2008). By

108 using numerical ocean models to examine the relationship between the NADW $\delta^{30}\text{Si}$ signature and the
109 pathways by which Si is transported by the MOC, this study assesses de Souza et al.'s (2012a)
110 hypothesis of large-scale controls on the Atlantic $\delta^{30}\text{Si}$ distribution, whilst also considering the
111 constraints placed by these observations on pathways of upwelling associated with the MOC.

112 *1.2. Support for a Southern Ocean control*

113 Support for a Southern Ocean control on the NADW $\delta^{30}\text{Si}$ signature is provided by the model
114 CYCLOPS, an ocean box model originally developed by Keir (1988) that has been modified to
115 explicitly represent the physical and biogeochemical zonation of the surface Southern Ocean (Fig. 2a;
116 Robinson et al., 2005; Hain et al., 2014b). A representation of the marine cycling of Si and its isotopes
117 (see Supplementary Information) allows an assessment of the leading-order sensitivities of the large-
118 scale $\delta^{30}\text{Si}$ distribution. As shown in Fig. 2b, the observed deep Atlantic Si concentration gradient
119 ($\sim 110 \mu\text{M}$) can be reproduced by simultaneously varying the length-scale defining the dissolution of
120 opal export (which determines the partitioning of opal dissolution between the intermediate and deep
121 ocean) and the degree of Si drawdown in the Subantarctic Zone (SAZ), from where the model's
122 Southern Ocean mode/intermediate waters are ventilated. In contrast, the gradient in $\delta^{30}\text{Si}$ between
123 NADW and the deep Southern Ocean is mostly insensitive to the opal dissolution length-scale, but
124 varies systematically with Si drawdown in the SAZ, disappearing when the Si concentration in the
125 SAZ is forced to zero, so as not to leave any residual high- $\delta^{30}\text{Si}$ in the SAZ surface (Fig. 2b). Under
126 these conditions, the model's advective pathway of Si supply from the surface Southern Ocean to the
127 high-latitude North Atlantic via mode/intermediate waters has been entirely eliminated, such that Si
128 can reach the North Atlantic solely via diffusive upward supply from the low-latitude deep ocean. This
129 sensitivity of the Atlantic $\delta^{30}\text{Si}$ gradient to Si supply by mode/intermediate waters supports the
130 hypothesis that it results from the cross-equatorial transport of a partial Si consumption signal from the
131 surface Southern Ocean. In the following, we further test this hypothesis by explicitly tracing the
132 origins of Si supplied to the North Atlantic by the large-scale ocean circulation in a suite of OGCMs in
133 which the pathways of deep water upwelling associated with the MOC are systematically varied.

134 *1.3. A theoretical framework*

135 Gnanadesikan's (1999; hereafter G99) analytical model of the volume balance of the oceanic
136 pycnocline (Fig. 3a) provides the conceptual basis for the OGCM suite presented in this study. This
137 model shows that the depth D of the pycnocline, separating the buoyant waters of the upper ocean
138 from the dense waters of the deep, results from the balance between four key processes that add or
139 remove buoyant water from the upper ocean. These processes are (i) the formation of deep water in the
140 North Atlantic (T_n in Fig. 3a), the balance between (ii) wind-driven upwelling and northward Ekman
141 transport in the Southern Ocean (T_w) and (iii) southward eddy-induced advection of light waters (T_e),
142 and (iv) low-latitude upwelling through the thermocline (T_u). There are two pathways by which
143 volume lost from the upper ocean during NADW formation can be replaced: (a) downward heat
144 transport driven by diapycnal mixing lightens dense waters, leading to an upwelling flux through the
145 thermocline; (b) Ekman divergence in the Southern Ocean drives the adiabatic upwelling of deep
146 waters, which are converted to lighter waters at the surface. G99 showed that the partitioning of
147 upwelling between these two pathways depends on diapycnal mixing and the advective effects of
148 eddies, represented by the diapycnal and isopycnal eddy diffusivities (κ_v and A_l) respectively. When
149 these diffusivities are small, both low-latitude upwelling T_u and the eddy return flow T_e compensating
150 northward Ekman transport T_w are minimal, such that deep upwelling (and the associated nutrient
151 supply) is driven by Ekman divergence in the surface Southern Ocean T_w (Fig. 3a). If, on the other
152 hand, A_l is large enough that the southward advective eddy transport in the Southern Ocean largely
153 compensates northward Ekman transport (i.e. if the net flux $T_w - T_e$ is small), most upwelling takes
154 place at low latitudes (T_u). This simultaneously requires high κ_v in order to maintain the observed
155 depth of the pycnocline against a large upwelling flux. This simple model thus makes an important
156 point: the pathway by which dissolved nutrients stored in the deep ocean return to the surface depends
157 on the vigorousness of turbulent mixing across and along density surfaces. By varying both these
158 parameters simultaneously in a numerical ocean model, we can produce widely varying pathways of
159 upwelling whilst maintaining the observed depth of the ocean's pycnocline. This study utilises three
160 variants of an OGCM with differing MOC pathways in order to systematically examine the
161 relationship between the $\delta^{30}\text{Si}$ signature of NADW and large-scale Si transport.

162

163 2. Methods

164 2.1. Model description and setup

165 The physical ocean model used is the Modular Ocean Model 3.0 (MOM3; Pacanowski and Griffies,
166 1999), run at $3.75^\circ \times 4.5^\circ$ horizontal resolution with 24 vertical levels. This primitive-equation OGCM
167 forms the basis of a model suite in which the values of diapycnal and isopycnal diffusivity are
168 systematically varied according to the theory of G99, so as to produce varying MOC pathways. This
169 suite is described in detail by Gnanadesikan et al. (2002, 2004, 2007) and Palter et al. (2010). In this
170 study, we employ model variants LL, HH and P2A, whose key variables are summarized in Table S1.
171 Model variant LL is a version of MOM3 in which both diapycnal and isopycnal eddy diffusivities
172 have low values. In LL, κ_v in the pycnocline is $1.5 \times 10^{-5} \text{ m}^2/\text{s}$, similar to values inferred from direct
173 tracer release experiments (Ledwell et al., 1993, 1998), increasing to $1.3 \times 10^{-4} \text{ m}^2/\text{s}$ at depth with a
174 hyperbolic tangent transition at 2500 m. Isopycnal diffusivity A_I , which is also the coefficient used in
175 the models' Gent–McWilliams parameterization of eddy thickness diffusion (Gent et al., 1995), has a
176 constant value of $1000 \text{ m}^2/\text{s}$ in LL. In model variant HH, in contrast, both κ_v and A_I have high values:
177 at $6 \times 10^{-5} \text{ m}^2/\text{s}$, pycnocline κ_v is four times higher than in LL, whilst the A_I of $2000 \text{ m}^2/\text{s}$ is twice as
178 large as in LL. Finally, model variant P2A conforms to observational constraints of low pycnocline
179 diffusivity (and thus has a pycnocline κ_v of $1.5 \times 10^{-5} \text{ m}^2/\text{s}$ and A_I of $1000 \text{ m}^2/\text{s}$, as in LL), but simulates
180 increased diapycnal mixing in the Southern Ocean, motivated by observations of high internal wave
181 activity there (Polzin et al., 1997). In addition to a number of specific changes relative to LL as listed
182 in Table S1 (and discussed by de Souza et al., 2014), P2A is forced by the ECMWF atmospheric
183 reanalysis of Trenberth et al. (1989), which imposes higher wind stresses over the Southern Ocean
184 than the reanalysis that forces LL and HH (Hellerman and Rosenstein, 1983).

185 The physical models are coupled to the nutrient-restoring biogeochemical model of Jin et al. (2006),
186 modified by de Souza et al. (2014) to include Si isotopes. As discussed therein, the model simulates
187 isotope fractionation during Si uptake in the surface ocean, but does not fractionate Si isotopes during
188 opal dissolution (Demarest et al., 2009; Wetzel et al., 2014; for a detailed discussion of this issue see
189 de Souza et al., 2014). Further diagnostics added for this study (Section 2.2) allow us to trace Si
190 originating from four high-latitude source regions in the models.

191 The simulations are initialized to steady-state physical conditions and distributions of Si and $\delta^{30}\text{Si}$
192 from a 5000-yr spin-up simulation for each model variant. The fractional contribution of each of the
193 four source regions (Section 2.2) to the Si inventory is initialized to a globally constant value of 25%,
194 and the simulations run forward for 2000 model years, by which time the Si source tracer distributions
195 achieve equilibrium. Targets for surface nutrient restoring are derived from the objectively-analysed
196 monthly climatologies of World Ocean Atlas 2009 (WOA09; Garcia et al., 2010). Results of the
197 simulations are presented as averages over the last 20 years of the simulations. We also present the
198 models' equilibrium (pre-bomb) radiocarbon distributions ($\Delta^{14}\text{C}$; Matsumoto et al., 2004) as 10-year
199 means.

200 2.2. Si source tagging scheme

201 In order to study the large-scale Si dynamics and transport in the model variants, we explicitly trace
202 four sources of Si, using the method of Palter et al. (2010). As defined in Fig. 4, we tag and trace Si
203 sourced from (a) the region of SAMW formation (*SAMW*), (b) the region of AAIW formation (*AAIW*),
204 (c) the deep Southern Ocean (*DEEP*), and (d) the subpolar North Pacific Ocean (*NPAC*). At every
205 model time step, Si within a defined source region is 'tagged' with the corresponding source identity.
206 For example, AAIW-derived Si is tagged between the $\sigma_{\theta} = 27.1$ and $\sigma_{\theta} = 27.4$ isopycnals south of
207 where the $\sigma_{\theta} = 26.5$ isopycnal shoals to 200m (see Fig. 4). Si tagged in this manner is transported
208 away from its source region by the circulation, and retains its source identity as it cycles through the
209 low latitude ocean and into the North Atlantic, our region of interest. Once acquired, source identity is
210 only destroyed when Si enters another source region: e.g., AAIW-derived Si flowing northward in the
211 surface Southern Ocean will lose its AAIW identity and be tagged as SAMW-sourced Si once it
212 crosses the instantaneous outcrop of the $\sigma_{\theta} = 27.1$ isopycnal. The sum of all four source tracers equals
213 the total pool of Si, allowing us to trace the fractional contribution of the source regions to the local Si
214 inventory at any point in the model. In the following, we refer to Si that has been tagged with a
215 particular source identity as being 'sourced' or 'derived' from that region (e.g. 'SAMW-derived').

216

217 3. Results

218 *3.1. MOC pathways, Si and $\delta^{30}\text{Si}$ distributions*

219 We begin by describing the upwelling pathways of the three model variants. Figure 3b shows the
220 zonally-averaged northward meridional volume transport above the $\sigma_\theta = 27.4$ isopycnal, which lies at
221 a depth of 800–1000 m at low latitudes in all models. An increase in horizontal transport implies
222 upwelling of water across this density surface, into the upper ocean. Thus, the differing latitudinal
223 evolution of this transport in the models reflects their differing MOC pathways. The constancy of
224 P2A’s meridional transport north of $\sim 50^\circ\text{S}$ shows that this model achieves most of its upwelling at
225 high southern latitudes (Fig. 3b). This Southern Ocean upwelling pathway is expected from G99 (Fig.
226 3a), given the low isopycnal and diapycnal diffusivities and the strong winds over the Southern Ocean
227 (Table S1): P2A not only restricts T_u through limited low-latitude diapycnal mixing and T_e through
228 low isopycnal diffusivity, but also has high T_w as a result of stronger Ekman transport in the Southern
229 Ocean. In contrast, volume transport in HH increases over a wide latitudinal band from $\sim 50^\circ\text{S}$ to
230 $\sim 30^\circ\text{N}$, reflecting low-latitude upwelling. The importance of low-latitude transport (T_u) for the
231 overturning is expected from G99, given HH’s high diffusivities and weaker Southern Ocean winds.
232 Model variant LL is intermediate between these two extremes, since southern upwelling extends
233 further north than in P2A, but limited low-latitude upwelling is implied by the constancy of meridional
234 volume transport north of $\sim 30^\circ\text{S}$. The overturning pathways simulated by LL and P2A are more
235 consistent with estimates from inverse models (Lumpkin and Speer, 2007) and the emerging view of
236 ocean overturning (Marshall and Speer, 2012; Talley, 2013), although LL’s ventilation of the deep
237 Southern and Pacific Oceans is too sluggish to accurately reproduce the $\Delta^{14}\text{C}$ distribution (Matsumoto
238 et al., 2004).

239 When combined with their shared biogeochemical model, which restores surface Si concentrations
240 towards observations, the circulation fields of the three models produce interior Si distributions that
241 reproduce the large-scale structure to the observed distribution, but also show differences both from
242 the observations and from each other. Figure 5 compares the models’ average Atlantic Si distribution
243 in the uppermost 2400m with WOA09 (see Fig. S3 for zonal averages). As in the observations, all
244 models exhibit a southward propagating tongue of low-Si NADW at mid-depth, and an intermediate-
245 depth tongue of elevated Si extending northwards from the Southern Ocean. However, in all model

246 variants, the low-Si tongue is too shallow, with a core at ~1600 m rather than ~1800m as in the
 247 observations. This is because North Atlantic convection in the models produces a water mass that is
 248 too light and thus descends to shallower depths than observed. As a result, the models' Si-rich AABW
 249 extends too far north, and upward diapycnal mixing of Si from this water mass leads to the elevated Si
 250 concentrations seen below ~2200m in all model variants. All models also overestimate Si in the
 251 northward-penetrating intermediate-depth tongue, a feature that is more pronounced in P2A and HH
 252 than in LL. The Si distribution of HH is least similar to the observations: the southward- and
 253 northward-propagating advective signals are much less clearly defined in this model than in LL or
 254 P2A, due to high interior diapycnal mixing. Model HH also strongly underestimates Si concentrations
 255 in the deep Southern Ocean relative to observations.

256 Despite these differences in the Si distribution between models, they display similar skill at
 257 reproducing the interior Atlantic $\delta^{30}\text{Si}$ distribution, especially in terms of its isotope systematics: as
 258 shown by Fig. 1a, all three models reproduce the near-linear $\delta^{30}\text{Si}-1/\text{Si}$ relationship observed in the
 259 deep Atlantic Ocean, simulate a similar range of $\delta^{30}\text{Si}$ variation in Atlantic deep waters, and reproduce
 260 the observation of elevated $\delta^{30}\text{Si}$ in the Si-poor deep North Atlantic. We will discuss the reasons for
 261 these similarities in Section 4. For now, bearing the differences in the Si distribution of the three
 262 models in mind, in the following we discuss the Si source tracer distributions in terms of their
 263 *fractional* contribution to the total Si inventory, $f(i) = [\text{Si}]_{\text{source}=i} / \sum_j [\text{Si}]_{\text{source}=j}$.

264 3.2. Si source tracer distributions

265 By examining the steady-state distributions of the Si source tracer contributions $f(i)$, we can study
 266 how Si from the four source regions spreads through the ocean to eventually contribute to the NADW
 267 Si inventory. We illustrate the influence of the models' differing MOC pathways on large-scale Si
 268 transport by examining the contribution of each source region to the Si inventory of the thermocline,
 269 which we define as the volume of water above the $\sigma_\theta = 26.8$ isopycnal.

270 The two sources of Si above the $\sigma_\theta = 26.8$ isopycnal, SAMW and NPAC, exhibit their maximal
 271 contributions to the thermocline Si inventory close to their source regions, from where Si is directly
 272 introduced into the thermocline (Fig. 6). The locus of maximum fraction of SAMW-derived Si,

273 $f(\text{SAMW})$, follows typical SAMW ventilation pathways (Sallée et al., 2010), extending anti-clockwise
274 into the subtropics from the southern outcrop (Fig. 6a). NPAC-sourced Si enters the North Pacific
275 thermocline from the north (Fig. 6d), and is transported into the Indian Ocean via the Indonesian
276 Throughflow, although virtually none enters the Atlantic via the warm-water pathway (Gordon, 1986)
277 without first entering the SAMW source region and losing its NPAC identity. NPAC-derived Si also
278 flows northward through Bering Strait, contributing considerably to the Si inventory of the Arctic
279 Ocean above $\sigma_\theta = 26.8$.

280 Silicon sourced from below the $\sigma_\theta = 26.8$ isopycnal (AAIW and DEEP) exhibits rather different
281 thermocline distributions, since it can enter the thermocline only via interior diapycnal fluxes across
282 this isopycnal. Thus, the contribution of AAIW- and DEEP-sourced Si increases towards the
283 subtropics and tropics, as deeper-lying Si is transported upwards (Fig. 6b,c). In concordance with the
284 models' differing MOC pathways, the contribution of DEEP-sourced Si to the thermocline inventory
285 is highest in the diffusive model HH, and is lowest in the more adiabatic P2A, whose thermocline is
286 also more vigorously ventilated along isopycnals from the south due to higher wind stress over the
287 Southern Ocean. The contribution of DEEP-sourced Si to the thermocline inventory is 1.3–1.6 times
288 higher in HH than in LL or P2A in the low-latitude Indian and Pacific Oceans, and even higher in the
289 Atlantic, where it can be more than twice as large in HH than in P2A (Fig. 6c). Complementarily, high
290 contributions of SAMW- and AAIW-derived Si penetrate further northward in LL and P2A than in
291 HH: high contributions of SAMW-derived Si extend well into the North Atlantic in LL and P2A, such
292 that $f(\text{SAMW})$ is 1.3–1.7 times higher in the tropical Atlantic thermocline of these models than in HH
293 (Fig. 6a). Additionally, the fraction of AAIW-derived Si in the Atlantic thermocline increases steadily
294 towards the north in LL and P2A but not in HH, such that in the North Atlantic subtropics, $f(\text{AAIW})$ in
295 P2A and LL is 1.2–1.5 times higher than in HH (Fig. 6b). In all three models, however, SAMW- and
296 AAIW-sourced Si together contribute at least half the Si inventory of the North Atlantic thermocline.

297 3.3. Diapycnal Si redistribution in the Atlantic Ocean

298 The consequences of northward transport of SAMW- and AAIW-derived Si for the source
299 composition of NADW are illustrated by Fig. 7, which shows the average source tracer contributions
300 $f(i)$ in the uppermost 2400m of the Atlantic Ocean (see Fig. S4 for zonal averages). Only SAMW-

301 derived Si spreads northwards at the surface, whilst Si from other source regions enters the Atlantic
302 within the interior. Diapycnal processes and biological cycling disperse Si from all four source regions
303 through the water column, e.g. the upward transport of DEEP-sourced Si into the thermocline, seen
304 most strongly in HH (Fig. 7c). However, diapycnal Si redistribution is reflected most dramatically by
305 the two source tracers that are tagged in the upper ocean according to density criteria, i.e. SAMW and
306 AAIW. The downward penetration of Si from these sources is greatest in the North Atlantic north of
307 40°N (Fig. 7a,b). A tongue of elevated $f(\text{SAMW})$ and $f(\text{AAIW})$ propagates southwards from these
308 high latitudes at about 1500-1600m, at densities significantly higher than those at which these tracers
309 are originally tagged (Fig. S5). This mid-depth tongue is the signal of NADW (Fig. 5), and reflects the
310 diapycnal transfer of Si sourced from the shallow Southern Ocean to deep water densities, due to
311 buoyancy loss in the subpolar North Atlantic, the Nordic Seas and the Arctic Ocean. The incorporation
312 of SAMW- and AAIW-derived Si into NADW takes place in all three model variants, although their
313 importance for its Si inventory varies, due to the differing extent of their transport to the shallow North
314 Atlantic. All three models also exhibit a deep (~1800m) tongue of NPAC-sourced Si extending
315 southwards from the subpolar North Atlantic (Fig. 7d). This is Si that has been transported from the
316 North Pacific via the Arctic Ocean, entering the North Atlantic through the models' representation of
317 the Nordic Sea overflows.

318

319 **4. Discussion**

320 The Si source tracer distributions reveal the pathways of large-scale Si transport and diapycnal
321 redistribution in the Atlantic Ocean. In the following, we focus on NADW flowing southward from
322 the subpolar North Atlantic, in order to elucidate the processes responsible for its unique $\delta^{30}\text{Si}$
323 signature.

324 *4.1. The isotopic signatures and source composition of NADW*

325 As indicated by the simulated Atlantic $\delta^{30}\text{Si}$ systematics (Fig. 1a), which show elevated $\delta^{30}\text{Si}$ values
326 associated with Si-poor waters of the deep North Atlantic, NADW appears prominently in the
327 simulated $\delta^{30}\text{Si}$ distribution as a high- $\delta^{30}\text{Si}$ tongue along the western boundary of the mid-depth North
328 Atlantic in all three models (Fig. 8a). The basin-scale structure of the simulated $\delta^{30}\text{Si}$ distributions is

329 broadly consistent with observations of elevated $\delta^{30}\text{Si}$ values ranging from +1.7 to +1.9‰ in the
330 western mid-depth North Atlantic (Fig. 1b; de Souza et al., 2012a; Brzezinski and Jones, 2015). Whilst
331 the less diffusive models P2A and LL reproduce the absolute $\delta^{30}\text{Si}$ values in NADW better than the
332 diffusive model HH (Figs. 8a,c), all three models reproduce the $\delta^{30}\text{Si}$ systematics of the deep Atlantic
333 with similar fidelity (Fig. 1a), although P2A simulates higher $\delta^{30}\text{Si}$ values in the subpolar North
334 Atlantic than LL or HH. It is interesting to note that the models reproduce the observed near-linear
335 $\delta^{30}\text{Si}$ systematics despite the fact that they do not simulate Si isotope fractionation during opal
336 dissolution. This contrasts somewhat with the recent study by Holzer and Brzezinski (2015), who
337 found that including this process improved the linearity of their model's Atlantic $\delta^{30}\text{Si}$ systematics by
338 increasing $\delta^{30}\text{Si}$ in the Si-richest Southern Ocean deep waters. Our results and theirs do, however,
339 agree in suggesting that fractionation during opal dissolution is not a major driver of the deep Atlantic
340 $\delta^{30}\text{Si}$ systematics.

341 Depth sections across $\sim 43^\circ\text{N}$ reveal the isotopic signal of NADW flowing around the Grand Banks
342 as a well-ventilated water mass: this freshly-ventilated NADW bears a $\Delta^{14}\text{C}$ maximum (Fig. 8b) and is
343 recognizable in the $\delta^{30}\text{Si}$ distribution by its elevated $\delta^{30}\text{Si}$ signature (Fig. 8c) in all models. These
344 isotopic distributions are closely mimicked by the fraction of Si sourced from SAMW and AAIW,
345 $f(\text{SAMW}+\text{AAIW})$ (Fig. 8d). The fractional contribution of SAMW- and AAIW-derived Si is highest
346 above the 27.4 isopycnal, in waters flowing towards the high-latitude North Atlantic in the upper limb
347 of the MOC. However, in each model, there is a secondary $f(\text{SAMW}+\text{AAIW})$ maximum at mid-depth,
348 coincident with the $\delta^{30}\text{Si}$ and $\Delta^{14}\text{C}$ signals of NADW. The fraction of NPAC-derived Si also shows a
349 maximum within this volume, but does not exceed 10% (Fig. S6d). Conversely, DEEP-sourced Si is at
350 its minimum within the freshly-ventilated NADW core (Fig. S6c). Thus, irrespective of the large-scale
351 circulation of the models, there is a clear spatial correlation between the maximum contribution of
352 SAMW- and AAIW-derived Si to NADW and the elevated $\delta^{30}\text{Si}$ signature observed in the most
353 recently ventilated deep waters (Figs. 8c,d and S7). We can quantify this relationship by calculating
354 the contributions of the source regions to the Si inventory of freshly-ventilated NADW.

355 Recently ventilated NADW exhibits clear signals of gas exchange with the atmosphere in the
356 models' radiocarbon and oxygen distributions (Figs. 8b, S1 and S2). We exploit these signals to define
357 a volume of freshly-ventilated NADW that extends from the shallow subpolar North Atlantic (>500m
358 water depth) to the equator along the western Atlantic boundary (Table 1; see also the Supplementary
359 Information). This allows us to calculate the integrated Si inventory of this volume and partition it
360 according to source region (Table 1). In all three model variants, SAMW and AAIW together
361 contribute a major or dominant fraction of the Si inventory, ranging from 46% in HH to 62% in P2A.
362 The importance of DEEP-sourced Si varies inversely with this contribution, whilst NPAC-derived Si
363 is of minor importance (5–9%) in all models.

364 The $\delta^{30}\text{Si}$ signature of the freshly-ventilated NADW volume rises systematically with the increase in
365 $f(\text{SAMW}+\text{AAIW})$ from HH to P2A, and ranges from +1.50‰ in HH to +1.74‰ in P2A (Table 1).
366 Thus, not only is there a clear spatial correlation between elevated values of $f(\text{SAMW}+\text{AAIW})$ and
367 $\delta^{30}\text{Si}$ *within* each model (Fig. S7), but also systematic co-variation *between* models: the greater the
368 SAMW/AAIW contribution to NADW, the higher its $\delta^{30}\text{Si}$ value. Together, these correlations strongly
369 suggest that cross-equatorial transport of Si that has been isotopically fractionated in the surface
370 Southern Ocean is instrumental in producing the high $\delta^{30}\text{Si}$ signature of NADW.

371 4.2. Distal and proximal fractionation controls on the NADW $\delta^{30}\text{Si}$ signature

372 The elevated $\delta^{30}\text{Si}$ signal of NADW is reproduced by all three models, despite their widely varying
373 MOC configurations. Whilst the analysis above indicates that this signal derives from the contribution
374 of SAMW/AAIW to NADW's Si inventory, we must also consider two additional factors that can
375 produce differences in the NADW $\delta^{30}\text{Si}$ signature between model variants. These are: (a) the isotopic
376 composition of Si exported from each source region, and (b) Si isotope fractionation at the ocean's
377 surface during transport from the source regions to the North Atlantic. In other words, the NADW
378 $\delta^{30}\text{Si}$ signature can be conceived of as resulting from a combination of the *conservative* transport of
379 isotope signatures from distal source regions, and the *non-conservative* alteration of these isotope
380 signatures en route. We can separate the effects of these two factors with a simple isotope mixing
381 calculation, allowing us to assess the extent to which the NADW $\delta^{30}\text{Si}$ signature is controlled by the

382 conservative transport of distal isotopic signals. We calculate the isotopic composition of Si within
 383 each source region (Table 1) as an estimate of the distal isotopic signals being exported towards the
 384 North Atlantic. Based on these values and the source tracer contributions at each model grid point, we
 385 can then calculate the $\delta^{30}\text{Si}$ distribution that would result simply from the spreading of these
 386 endmember $\delta^{30}\text{Si}$ signatures:

$$387 \quad \delta^{30}\text{Si}_{\text{distal}} = \sum_i f(i) \cdot \delta^{30}\text{Si}_{i,\text{source}} \quad (\text{Eqn. 1})$$

388 where $f(i)$ is the local fractional contribution of the source i , and $\delta^{30}\text{Si}_{i,\text{source}}$ is the isotopic
 389 composition in the source region i . We hasten to note that this approach makes the simplifying
 390 assumption that Si supplied from each source region has a uniform $\delta^{30}\text{Si}$ value, which is not the case.
 391 However, as we show below, it nonetheless serves to provide us with a useful estimate of the influence
 392 of the large-scale transport of isotope signals.

393 The meridional sections in Fig. 9 compare the simulated Atlantic $\delta^{30}\text{Si}$ distribution at 25°W (Fig.
 394 9a) with the $\delta^{30}\text{Si}_{\text{distal}}$ distribution (Fig. 9b). It can be seen that in all three model variants, considerable
 395 large-scale interior Atlantic $\delta^{30}\text{Si}$ variability, including an elevated NADW $\delta^{30}\text{Si}$ signature, is
 396 predicted to result simply from the propagation of distal source-region $\delta^{30}\text{Si}$ signals. Furthermore, as
 397 shown by the close correlation between the two fields (Fig. 9d), the structure of the $\delta^{30}\text{Si}_{\text{distal}}$
 398 distribution bears a strong resemblance to the simulated $\delta^{30}\text{Si}$ field. These results indicate that the
 399 long-range transport of isotope signals plays a significant role in determining the basin-scale $\delta^{30}\text{Si}$
 400 distribution. However, in all cases the range in $\delta^{30}\text{Si}_{\text{distal}}$ is muted in comparison to the simulated field
 401 (slopes < 1 in Fig. 9d), with $\delta^{30}\text{Si}_{\text{distal}}$ values generally lower than simulated values in the upper ocean
 402 (Fig. 9c). This is reflected in the $\delta^{30}\text{Si}_{\text{distal}}$ signature of the freshly-ventilated NADW volume, which
 403 underestimates the simulated $\delta^{30}\text{Si}$ value by 0.13–0.22‰ (Table 1).

404 Two reasons for the mismatch between $\delta^{30}\text{Si}_{\text{distal}}$ and simulated $\delta^{30}\text{Si}$ become clear upon closer
 405 inspection of Fig. 9. Firstly, the assumption of uniform source $\delta^{30}\text{Si}$ values in Eqn. 1 ignores the
 406 significant isotopic variability within each source region. This simplification results, for example, in
 407 the northward propagation of too-low $\delta^{30}\text{Si}_{\text{distal}}$ values from the Southern Ocean just below the $\sigma_\theta =$

408 27.4 isopycnal in all models, reflected by the bolus of elevated mismatch at this location in all models
409 (Fig. 9c). Secondly, a clear difference between $\delta^{30}\text{Si}$ and $\delta^{30}\text{Si}_{distal}$ is observed in the near-surface
410 ocean, where the simulated $\delta^{30}\text{Si}$ field exhibits high values throughout the low latitudes and in the
411 subpolar North Atlantic (Fig. 9a), whilst $\delta^{30}\text{Si}_{distal}$ values in the uppermost 500m decrease considerably
412 from the southern tropics northwards (Fig. 9b). This change is seen mostly clearly at the level of
413 SAMW in all models (Fig. 9c), where the sign of mismatch between the two fields changes from
414 negative ($\delta^{30}\text{Si}_{distal} > \delta^{30}\text{Si}$) to positive ($\delta^{30}\text{Si} > \delta^{30}\text{Si}_{distal}$) towards the north. The decoupling of $\delta^{30}\text{Si}_{distal}$
415 from $\delta^{30}\text{Si}$ during northward transport in the upper ocean is the result of two opposing tendencies. A
416 decrease in $\delta^{30}\text{Si}_{distal}$ is driven by the upward transport of AAIW- and DEEP-sourced Si in the low-
417 latitude ocean (Figs. 7 and 8), pools that have significantly lower $\delta^{30}\text{Si}$ values than SAMW-sourced Si
418 (Table 1). In contrast, an elevation of simulated $\delta^{30}\text{Si}$ values in the upper ocean results from isotope
419 fractionation during Si utilisation in the low latitude ocean and the subpolar North Atlantic. This
420 fractionation directly affects $\delta^{30}\text{Si}$ values in the surface ocean, but also more indirectly elevates near-
421 surface $\delta^{30}\text{Si}$ via the subduction of a high- $\delta^{30}\text{Si}$ signal into the subtropical North Atlantic thermocline.
422 Thus, some fraction of the difference between the $\delta^{30}\text{Si}$ and $\delta^{30}\text{Si}_{distal}$ fields results from the isotope
423 fractionation of Si within the Atlantic Ocean.

424 This result implies that the elevated NADW $\delta^{30}\text{Si}$ signature simulated by the models is not simply
425 the result of distal fractionation in the surface Southern Ocean, but also reflects more proximal isotope
426 fractionation as Si is transported towards the NADW formation region in the upper limb of the MOC,
427 i.e. the *non-conservative* effect discussed above. The offset between the $\delta^{30}\text{Si}$ and $\delta^{30}\text{Si}_{distal}$ fields is
428 much smaller at the depth of NADW than in the upper ocean (Fig. 9a,b), showing that the signal of
429 proximal fractionation is damped during NADW formation. This is due to the importance of Si-richer
430 subsurface waters, whose Si inventory is not exposed to isotope fractionation in the surface, in
431 determining the NADW $\delta^{30}\text{Si}$ value (cf. Sigman et al., 2000).

432 Due to the uncertainty introduced into our calculation of $\delta^{30}\text{Si}_{distal}$ by the assumption of constant
433 source region $\delta^{30}\text{Si}$ signatures, we can only provide an estimate of the extent of the proximal
434 modulation of distal isotope signals. A useful metric for this estimation is the deep Atlantic $\delta^{30}\text{Si}$

435 gradient, i.e. the difference between the $\delta^{30}\text{Si}$ values of NADW and AABW. The three model variants
436 produce Atlantic deep water $\delta^{30}\text{Si}$ differences of varying strength, ranging from 0.31‰ in HH to
437 0.63‰ in P2A (Table 1), compared to an observed difference of $\sim 0.5\%$ (de Souza et al., 2012a). By
438 assessing what proportion of this basin-scale $\delta^{30}\text{Si}$ difference is explained by the $\delta^{30}\text{Si}_{\text{distal}}$ signature of
439 NADW, we can estimate the fraction that results simply from the propagation of source-region $\delta^{30}\text{Si}$
440 signatures. The results shown in Table 1 reveal that this conservative effect explains 54% to 80% of
441 the deep Atlantic $\delta^{30}\text{Si}$ gradient. Our simulations thus indicate that the high $\delta^{30}\text{Si}$ value of NADW, and
442 indeed the basin-scale $\delta^{30}\text{Si}$ distribution, is largely governed by the transport of distal surface Southern
443 Ocean isotope signatures to the North Atlantic in SAMW and AAIW, as postulated by de Souza et al.
444 (2012a).

445 *4.3. Compensatory mechanisms in the Atlantic $\delta^{30}\text{Si}$ systematics*

446 The above discussion of the distal and proximal controls on the $\delta^{30}\text{Si}$ distribution also helps
447 elucidate the mechanisms by which the models all produce an elevated NADW $\delta^{30}\text{Si}$ signal, despite
448 differing pathways of deep water upwelling. The importance of the cross-equatorial transport of distal
449 isotopic signals in producing the Atlantic $\delta^{30}\text{Si}$ gradient differs between the models, and is least in the
450 highly diffusive model HH, which upwells more interior Si to the surface in the low latitudes (Table
451 1). This relationship suggests that there are compensatory mechanisms at play in the models' Atlantic
452 $\delta^{30}\text{Si}$ systematics: the more diffusive model HH advects less fractionated Si to the North Atlantic from
453 the surface Southern Ocean (Figs. 6–8), but produces a high- $\delta^{30}\text{Si}$ signal more proximally through
454 fractionation of more vigorously supplied deeply-sourced Si in the low-latitude or subarctic Atlantic
455 (Fig. 9), allowing it to produce NADW with a high $\delta^{30}\text{Si}$ value. Conversely, the more adiabatic models
456 P2A and LL favour distal control on the elevated $\delta^{30}\text{Si}$ of NADW. The models thus trade off between
457 distal and proximal isotope fractionation as a means of supplying isotopically fractionated Si to the
458 NADW formation region. It is this compensation that allows all three models to produce Atlantic $\delta^{30}\text{Si}$
459 systematics that are remarkably similar to observations (Fig. 1a), despite their widely-varying MOC
460 pathways. The existence of these interacting controls on the NADW $\delta^{30}\text{Si}$ signature also means that
461 the presence of an Atlantic $\delta^{30}\text{Si}$ gradient cannot be uniquely tied to fractionation in the high-latitude

462 Southern Ocean, as suggested by de Souza et al. (2012a). As a result, our simulations indicate that this
463 isotopic feature does not constrain the pathways by which deep water is returned to the upper ocean in
464 the MOC.

465 More generally, the results of our study contribute to an emerging picture of the role of Southern
466 Ocean Si isotope “distillation” (Brzezinski and Jones, 2015) in governing the marine $\delta^{30}\text{Si}$ distribution.
467 This distillation results from the combined physical and biogeochemical dynamics of the Southern
468 Ocean, and leads to the trapping of low- $\delta^{30}\text{Si}$ silicic acid in the deep Southern Ocean (Holzer et al.,
469 2014; Holzer and Brzezinski, 2015) coupled to a complementary northward export of a high- $\delta^{30}\text{Si}$
470 signature in SAMW/AAIW (Fripiat et al., 2011; de Souza et al., 2012b). de Souza et al. (2014) have
471 recently shown that the isotopically light preformed and regenerated Si in the deep Southern Ocean is
472 spread throughout the global abyssal ocean by AABW, producing the observed hydrographic control
473 on the deep $\delta^{30}\text{Si}$ distribution. This study has highlighted the large-scale influence of the
474 complementary high $\delta^{30}\text{Si}$ signal exported in SAMW/AAIW, showing that the Southern Ocean
475 influences the global $\delta^{30}\text{Si}$ distribution by two separate pathways associated with the upper *and* lower
476 limbs of the MOC. However, consistent with the recent study by Holzer and Brzezinski (2015), our
477 results also allow a role for fractionation during low-latitude Si cycling in determining the large-scale
478 $\delta^{30}\text{Si}$ distribution, indicating that other ocean regions may modulate the signals exported from the
479 Southern Ocean.

480 An important open question that our study does not explicitly address is the role of the Arctic
481 Ocean, which Brzezinski and Jones (2015) have suggested may represent an important northern
482 counterpart to the Southern Ocean, via its influence on the Nordic Sea overflows. The Arctic Ocean
483 receives fractionated Si primarily through shallow inflow from the North Atlantic, and transfers this Si
484 to deep-water densities via buoyancy loss (Jones et al., 1995). Certainly some of the SAMW/AAIW-
485 sourced Si in our models’ NADW has been incorporated in this manner. What remains to be assessed
486 is whether the Arctic Ocean’s role is limited to such diapycnal Si transfer, or whether a significant
487 additional fractionation signal is imposed by Si cycling within the Arctic itself. Answering this
488 question will require the long-overdue analysis of the Arctic $\delta^{30}\text{Si}$ distribution.

489

490 **5. Conclusions**

491 This study has combined models of the marine cycle of Si and its isotopes with a diagnostic scheme
492 that enables us to trace the large-scale transport of Si originating from the high-latitude ocean in a
493 suite of OGCM simulations with varying MOC pathways. These simulations allow an assessment of
494 the role of cross-equatorial transport of SAMW- and AAIW-derived Si in producing the elevated $\delta^{30}\text{Si}$
495 signature of NADW. We find that Si sourced from the SAMW and AAIW formation regions
496 contributes a major to dominant fraction (46-62%) of the freshly-ventilated NADW Si inventory
497 irrespective of MOC pathway, and that the $\delta^{30}\text{Si}$ signature of NADW rises as the contribution of
498 SAMW- and AAIW-derived Si increases. However, the simulations also indicate that more proximal
499 isotope fractionation of Si, within the low-latitude or subpolar North Atlantic, can influence the
500 NADW $\delta^{30}\text{Si}$ signature. By revealing this interplay between distal and proximal processes, our results
501 thus allow us to refine the hypothesis of de Souza et al. (2012a): the high $\delta^{30}\text{Si}$ signature of NADW is
502 vitally linked to the transport of a fractionated signal from the surface Southern Ocean by
503 SAMW/AAIW, but may also be additionally influenced by Si isotope fractionation that takes place
504 during transport to the NADW formation region. The more adiabatic models in our suite, which
505 conform best to our current understanding of deep-water upwelling pathways (e.g. Talley, 2013),
506 suggest that the proximal contribution is small, although definitive conclusions remain elusive given
507 lingering uncertainties regarding the pathways of the MOC (e.g. Talley, 2008).

508

509 **Acknowledgements**

510 The authors gratefully acknowledge helpful comments on an earlier version of this manuscript by
511 Timothy Conway and Beatrice Radden Keefe, and the constructive reviews of two anonymous
512 reviewers. This work was supported by Swiss National Science Foundation post-doctoral fellowships
513 PBEZP2-140169 and P300P2-147747 granted to GFDS, NOAA grant NA11OAR4310066 to JLS, and
514 UK NERC grant NE/K00901X/1 to MPH.

515

516 **References**

- 517 Abouchami, W., Galer, S. J. G., de Baar, H. J. W., Middag, R., Vance, D., Zhao, Y., et al., 2014.
518 Biogeochemical cycling of cadmium isotopes in the Southern Ocean along the Zero Meridian.
519 *Geochim. Cosmochim. Acta* 127, 348-367.
- 520 Broecker, W. S., Peng, T. H., 1982. *Tracers In The Sea*. Eldigio Press/Lamont-Doherty Geological
521 Observatory, Palisades, NY.
- 522 Broecker, W.S., Blanton, S., Smethie, W.M., Ostlund, G., 1991. Radiocarbon decay and oxygen
523 utilization in the deep Atlantic Ocean. *Glob. Biogeochem. Cyc.* 5, 87-117.
- 524 Brzezinski, M. A., Dickson, M. L., Nelson, D. M., Sambrotto, R., 2003. Ratios of Si, C and N uptake
525 by microplankton in the Southern Ocean. *Deep-Sea Res. II* 50, 619-633.
- 526 Brzezinski, M. A., Jones, J. L., 2015. Coupling of the distribution of silicon isotopes to the meridional
527 overturning circulation of the North Atlantic Ocean. *Deep Sea Res. II* 116, 79-88.
- 528 Buesseler, K. O., 1998. The decoupling of production and particulate export in the surface ocean.
529 *Glob. Biogeochem. Cyc.* 12, 297-310.
- 530 Cardinal, D., Alleman, L. Y., Dehairs, F., Savoye, N., Trull, T. W., Andre, L., 2005. Relevance of
531 silicon isotopes to Si-nutrient utilization and Si-source assessment in Antarctic waters. *Glob.*
532 *Biogeochem. Cyc.* 19, doi: 10.1029/2004GB002364.
- 533 De La Rocha, C. L., Brzezinski, M. A., DeNiro, M. J., 1997. Fractionation of silicon isotopes by
534 marine diatoms during biogenic silica formation. *Geochim. Cosmochim. Acta* 61, 5051-5056.
- 535 Demarest, M. S., Brzezinski, M. A., Beucher, C. P., 2009. Fractionation of silicon isotopes during
536 biogenic silica dissolution. *Geochim. Cosmochim. Acta* 73, 5572-5583.
- 537 de Souza, G. F., Reynolds, B. C., Rickli, J., Frank, M., Saito, M. A., Gerringa, L. J. A., et al., 2012a.
538 Southern Ocean control of silicon stable isotope distribution in the deep Atlantic Ocean. *Glob.*
539 *Biogeochem. Cyc.* 26, doi: 10.1029/2011gb004141.
- 540 de Souza, G. F., Reynolds, B. C., Johnson, G. C., Bullister, J. L., Bourdon, B., 2012b. Silicon stable
541 isotope distribution traces Southern Ocean export of Si to the eastern South Pacific thermocline.
542 *Biogeosci.* 9, 4199-4213.

543 de Souza, G. F., Slater, R. D., Dunne, J. P., Sarmiento, J. L., 2014. Deconvolving the controls on the
544 deep ocean's silicon stable isotope distribution. *Earth Planet. Sci. Lett.* 398, 66-76.

545 Fripiat, F., Cavagna, A.-J., Dehairs, F., Speich, S., André, L., Cardinal, D., 2011. Silicon pool
546 dynamics and biogenic silica export in the Southern Ocean, inferred from Si-isotopes. *Ocean Sci.* 7,
547 533-547.

548 Garcia, H. E., Locarnini, R. A., Boyer, T. P., Antonov, J. I., 2010. *World Ocean Atlas 2009, Volume 4:*
549 *Nutrients (phosphate, nitrate, silicate)*. U.S. Government Printing Office, Washington DC.

550 Gent, P. R., Willebrand, J., McDougall, T. J., McWilliams, J. C., 1995. Parametrizing eddy-induced
551 tracer transports in ocean circulation models. *J. Phys. Oceanogr.* 25, 463-474.

552 Gnanadesikan, A., 1999. A simple predictive model for the structure of the oceanic pycnocline.
553 *Science* 283, 2077-2079.

554 Gnanadesikan, A., Slater, R. D., Gruber, N., Sarmiento, J. L., 2002. Oceanic vertical exchange and
555 new production: a comparison between models and observations. *Deep Sea Res. II* 49, 363-401.

556 Gnanadesikan, A., Dunne, J., Key, R., Matsumoto, K., Sarmiento, J. L., Slater, R., et al., 2004.
557 Oceanic ventilation and biogeochemical cycling: Understanding the physical mechanisms that
558 produce realistic distributions of tracers and productivity. *Glob. Biogeochem. Cyc.* 18, doi:
559 10.1029/2003GB002097.

560 Gnanadesikan, A., De Boer, A. M., Mignone, B. K., 2007. A simple theory of the pycnocline and
561 overturning revisited. In: Schmittner, A., Chiang, J. C. H., and Hemming, S., (Eds.), *Ocean*
562 *Circulation: Mechanisms and Impacts—Past and Future Changes of Meridional Overturning*.
563 American Geophysical Union, pp 19-32.

564 Gordon, A. L., 1986. Interocean exchange of thermocline water. *J. Geophys. Res. Ocean.* 91, 5037-
565 5046.

566 Grasse, P., Ehlert, C., Frank, M., 2013. The influence of water mass mixing on the dissolved Si
567 isotope composition in the Eastern Equatorial Pacific. *Earth Planet. Sci. Lett.* 380, 60-71.

568 Hain, M. P. Sigman, D. M, Haug, G. H., 2014a. The biological pump in the past, in: Holland, H. and
569 Turekian, K. K. (Eds.), *Treatise on Geochemistry*, second ed. Elsevier, Amsterdam, pp. 485-517.

570 Hain, M. P., Sigman, D. M., Haug, G. H., 2014b. Distinct roles of the Southern Ocean and North
571 Atlantic in the deglacial atmospheric radiocarbon decline. *Earth Planet. Sci. Lett.* 394, 198-208.

572 Hellerman, S., Rosenstein, M., 1983. Normal monthly wind stress over the world ocean with error
573 estimates. *J. Phys. Oceanogr.* 13, 1093-1104.

574 Holzer, M., Primeau, F. W., DeVries, T., Matear, R., 2014. The Southern Ocean silicon trap: data-
575 constrained estimates of regenerated silicic acid, trapping efficiencies, and global transport paths. *J.*
576 *Geophys. Res. Ocean.* 119, doi: 10.1002/2013jc009356.

577 Holzer, M., Brzezinski, M. A., 2015. Controls on the silicon isotope distribution in the ocean: new
578 diagnostics from a data-constrained model. *Glob. Biogeochem. Cyc.* 29, doi:
579 10.1002/2014GB004967.

580 Jin, X., Gruber, N., Dunne, J. P., Sarmiento, J. L., Armstrong, R. A., 2006. Diagnosing the
581 contribution of phytoplankton functional groups to the production and export of particulate organic
582 carbon, CaCO₃, and opal from global nutrient and alkalinity distributions. *Glob. Biogeochem. Cyc.*
583 20, doi: 10.1029/2005GB002532.

584 Jones, E. P., Rudels, B., Anderson, L. G., 1995. Deep waters of the Arctic Ocean: origins and
585 circulation. *Deep Sea Res. I* 42, 737-760.

586 Karleskind, P., Lévy, M., Memery, L., 2011. Subduction of carbon, nitrogen, and oxygen in the
587 northeast Atlantic. *J. Geophys. Res. Ocean.* 116, doi: 10.1029/2010jc006446.

588 Keir, R. S., 1988. On the Late Pleistocene ocean geochemistry and circulation. *Paleoceanogr.* 3, 413-
589 455.

590 Ledwell, J. R., Watson, A. J., Law, C. S., 1993. Evidence for slow mixing across the pycnocline from
591 an open-ocean tracer-release experiment. *Nature* 364, 701-703.

592 Ledwell, J. R., Watson, A. J., Law, C. S., 1998. Mixing of a tracer in the pycnocline. *J. Geophys. Res.*
593 *Ocean.* 103, 21,499–21,529.

594 Lumpkin, R., Speer, K., 2007. Global ocean meridional overturning. *J. Phys. Oceanogr.* 37, 2550-
595 2562.

596 Marinov, I., Gnanadesikan, A., Toggweiler, J. R., Sarmiento, J. L., 2006. The Southern Ocean
597 biogeochemical divide. *Nature* 441, 964-967.

598 Marshall, J., Speer, K., 2012. Closure of the meridional overturning circulation through Southern
599 Ocean upwelling. *Nature Geosci.* 5, 171-180.

600 Matsumoto, K., Sarmiento, J. L., Key, R. M., Aumont, O., Bullister, J. L., Caldeira, K., et al., 2004.
601 Evaluation of ocean carbon cycle models with data-based metrics. *Geophys. Res. Lett.* 31, doi:
602 10.1029/2003gl018970.

603 Morrison, A.K., Fröhlicher, T.L., Sarmiento, J.L., 2015. Upwelling in the Southern Ocean. *Physics*
604 *Today* 68, doi: 10.1063/PT.1063.2654.

605 Pacanowski, R. C., Griffies, S. M., 1999. *The MOM3.0 Manual*, NOAA/Geophysical Fluid Dynamics
606 Laboratory, Princeton.

607 Palter, J. B., Lozier, M. S., Barber, R. T., 2005. The effect of advection on the nutrient reservoir in the
608 North Atlantic subtropical gyre. *Nature* 437, 687-692.

609 Palter, J. B., Sarmiento, J. L., Gnanadesikan, A., Simeon, J., Slater, R. D., 2010. Fueling export
610 production: nutrient return pathways from the deep ocean and their dependence on the meridional
611 overturning circulation. *Biogeosci.* 7, 3549-3568.

612 Palter, J. B., Lozier, M. S., Sarmiento, J. L., Williams, R. G., 2011. The supply of excess phosphate
613 across the Gulf Stream and the maintenance of subtropical nitrogen fixation. *Glob. Biogeochem.*
614 *Cyc.* 25, doi: 10.1029/2010GB003955.

615 Polzin, K. L., Toole, J. M., Ledwell, J. R., Schmitt, R. W., 1997. Spatial variability of turbulent mixing
616 in the abyssal ocean. *Science* 276, 93-96.

617 Raven, J. A., 1983. The transport and function of silicon in plants. *Biol. Rev.* 58, 179-207.

618 Reynolds, B. C., Frank, M., Halliday, A. N., 2006. Silicon isotope fractionation during nutrient
619 utilization in the North Pacific. *Earth Planet. Sci. Lett.* 244, 431-443.

620 Robinson, A., Stommel, H., 1959. The oceanic thermocline and the associated thermohaline
621 circulation. *Tellus* 11, 295-308.

622 Robinson, R. S., Sigman, D. M., DiFiore, P. J., Rohde, M. M., Mashiotta, T. A., Lea, D. W., 2005.
623 Diatom-bound $^{15}\text{N}/^{14}\text{N}$: new support for enhanced nutrient consumption in the ice age Subantarctic.
624 *Paleoceanogr.* 20, doi: 10.1029/2004pa001114.

625 Sarmiento, J. L., Gruber, N., Brzezinski, M. A., Dunne, J. P., 2004. High-latitude controls of
626 thermocline nutrients and low latitude biological productivity. *Nature* 427, 56-60.

627 Sarmiento, J. L., Simeon, J., Gnanadesikan, A., Gruber, N., Key, R. M., Schlitzer, R., 2007. Deep
628 ocean biogeochemistry of silicic acid and nitrate. *Glob. Biogeochem. Cyc.* 21,
629 doi:10.1029/2006GB002720.

630 Sallée, J.-B., Speer, K., Rintoul, S., Wijffels, S., 2010. Southern Ocean thermocline ventilation. *J.*
631 *Phys. Oceanogr.* 40, 509-529.

632 Sigman, D. M., Altabet, M. A., McCorkle, D. C., François, R., Fischer, G., 2000. The $\delta^{15}\text{N}$ of nitrate
633 in the Southern Ocean: nitrogen cycling and circulation in the ocean interior. *J. Geophys. Res.*
634 *Ocean.* 105, 19599-19614.

635 Smetacek, V., 1999. Diatoms and the ocean carbon cycle. *Protist* 150, 25-32.

636 Sutton, J. N., Varela, D. E., Brzezinski, M. A., Beucher, C. P., 2013. Species-dependent silicon isotope
637 fractionation by marine diatoms. *Geochim. Cosmochim. Acta* 104, 300-309.

638 Talley, L. D., 2008. Freshwater transport estimates and the global overturning circulation: Shallow,
639 deep and throughflow components. *Prog. Oceanogr.* 78, 257-303.

640 Talley, L. D., 2013. Closure of the global overturning circulation through the Indian, Pacific, and
641 Southern Oceans: schematics and transports. *Oceanogr.* 26, 80-97.

642 Talley, L. D., Reid, J. L., Robbins, P. E., 2003. Data-based meridional overturning streamfunctions for
643 the global ocean. *J. Clim.* 16, 3213-3226.

644 Toggweiler, J. R., Samuels, B., 1993. New radiocarbon constraints on the upwelling of abyssal water
645 to the ocean's surface, in: Heimann, M., (Ed.), *The Global Carbon Cycle*. Springer, Berlin, pp. 333-
646 366.

647 Tréguer, P. J., De La Rocha, C. L., 2013. The world ocean silica cycle. *Ann. Rev. Mar. Sci.* 5, 477-
648 501.

649 Trenberth, K. E., Olson, J., Large, W., 1989. *A global ocean wind stress climatology based on*
650 *ECMWF analyses*. Technical Report NCAR/TN-338+STR, National Center for Atmospheric
651 Research, Boulder, CO.

652 Wetzel, F., de Souza, G. F., Reynolds, B. C., 2014. What controls silicon isotope fractionation during
653 dissolution of diatom opal? *Geochim. Cosmochim. Acta* 131, 128-137.
654

655 **Table 1: Quantification of Si source contributions to freshly-ventilated NADW. Threshold values**
656 **of $\Delta^{14}\text{C}$ and $[\text{O}_2]$ used to define the volume of freshly-ventilated North Atlantic Deep Water (see**
657 **Supplementary Information) in the model variants used in this study, together with integrated**
658 **$\delta^{30}\text{Si}$ signature and contributions of the four source regions to the Si inventory of this volume.**

	HH	LL	P2A
Radiocarbon threshold [‰]	-70	-70	-80
Oxygen threshold [mmol/m ³]	260	260	240
<i>Properties of the NADW volume:</i>			
NADW $\delta^{30}\text{Si}$ [‰]	+1.50	+1.66	+1.74
<i>f</i> (SAMW)	0.166	0.124	0.267
<i>f</i> (AAIW)	0.292	0.368	0.348
<i>f</i>(SAMW+AAIW)	0.457	0.491	0.615
<i>f</i> (DEEP)	0.484	0.419	0.331
<i>f</i> (NPAC)	0.059	0.090	0.054
<i>Source-region isotope signatures:</i>			
SAMW $\delta^{30}\text{Si}$ [‰]	+1.71	+2.07	+2.31
AAIW $\delta^{30}\text{Si}$ [‰]	+1.37	+1.47	+1.52
DEEP $\delta^{30}\text{Si}$ [‰]	+1.19	+1.18	+1.15
NPAC $\delta^{30}\text{Si}$ [‰]	+1.62	+1.66	+1.57
<i>Source-region signature propagation (Eqn. 1):</i>			
NADW $\delta^{30}\text{Si}_{\text{distal}}$ [‰]	+1.35	+1.44	+1.61
NADW $\delta^{30}\text{Si}_{\text{distal}} - \text{NADW } \delta^{30}\text{Si}$ [‰]	-0.14	-0.22	-0.13
<i>Deep Atlantic $\delta^{30}\text{Si}$ gradient:</i>			
AABW $\delta^{30}\text{Si}$ [‰]	+1.18	+1.16	+1.10
NADW $\delta^{30}\text{Si} - \text{AABW } \delta^{30}\text{Si}$ [‰]	0.31	0.50	0.64
NADW $\delta^{30}\text{Si}_{\text{distal}} - \text{AABW } \delta^{30}\text{Si}$ [‰]	0.17	0.28	0.51
Fraction of $\delta^{30}\text{Si}$ difference explained by $\delta^{30}\text{Si}_{\text{distal}}$	54%	56%	80%

Fig. 1: Silicon isotope data from the Atlantic Ocean. (a) Data from the deep (>2000m) Atlantic Ocean from latitudes ranging from ~60°N to ~60°S in isotope mixing space (de Souza et al., 2012a), illustrating the systematic variation of deep water $\delta^{30}\text{Si}$ values. The near-linear relationship between $\delta^{30}\text{Si}$ and $1/[\text{Si}]$ indicates quasi-conservative mixing of Si brought into the deep Atlantic by Si-rich Southern Ocean sources (CDW) as well as Si-poor North Atlantic (LSW) and Nordic (DSOW, ISOW) sources. Open red symbols are results from the OGCMs used in this study (see Section 2.1), subsampled at the observational sampling locations. (b) Depth profiles of $\delta^{30}\text{Si}$ from the GEOTRACES North Atlantic Zonal Transect at 20°–40°N (Brzezinski and Jones, 2015) reveal the elevated $\delta^{30}\text{Si}$ values associated with the southward transport of NADW at mid-depths in the western Atlantic Ocean (blue and green points; see inset).

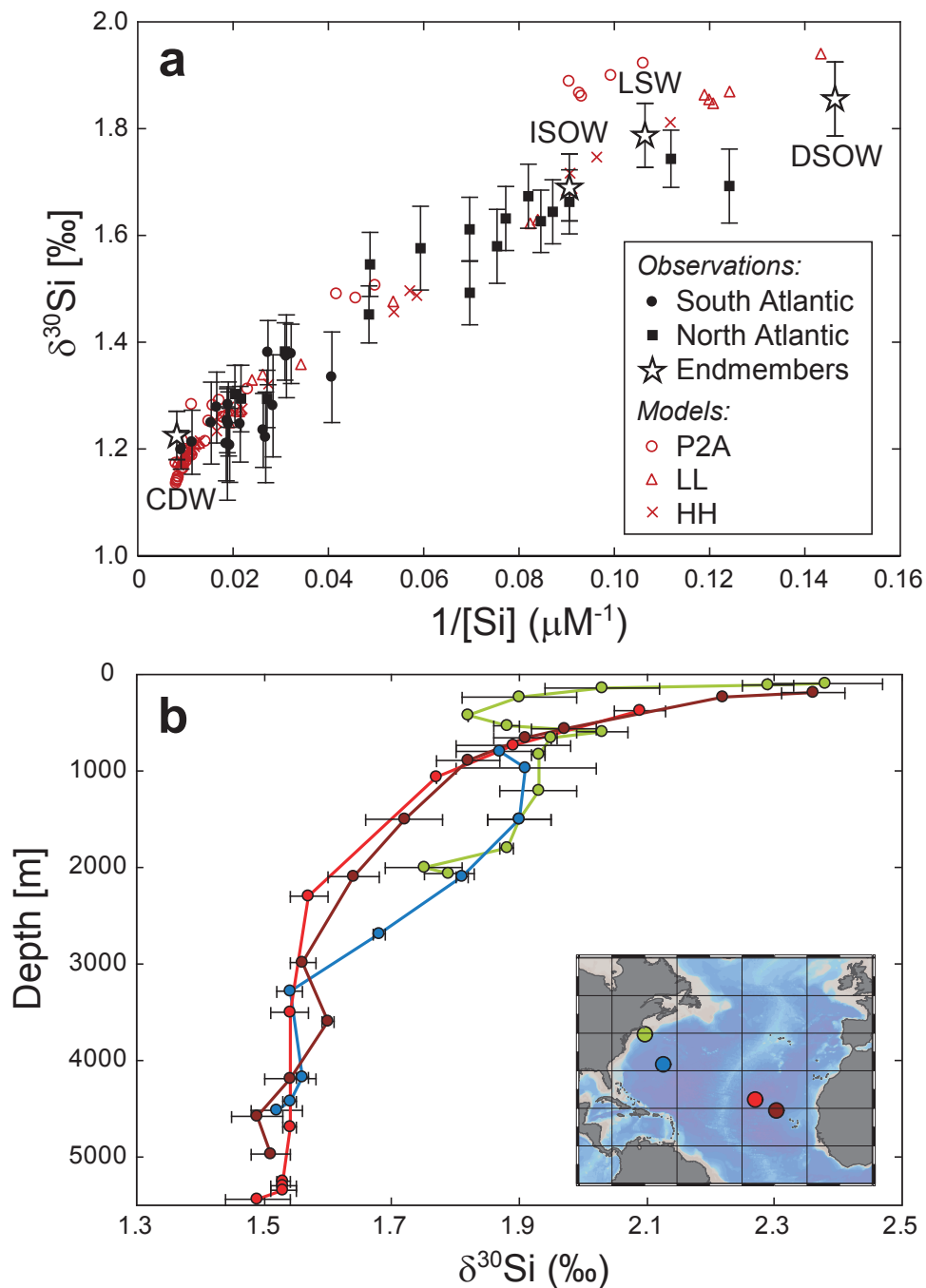


Fig. 2: (a) Schematic representation of the Atlantic circulation in the CYCLOPS ocean box model (Hain et al., 2014b), highlighting advective (black arrows) and “diffusive” exchange (red arrows) fluxes. In the sensitivity study discussed in the text (Section 1.2), the Si concentration of the Subantarctic surface box (light red shading) was systematically varied together with the length scale of opal dissolution, which controls the fraction of the sinking opal flux exported to the deep ocean boxes. The results of these parameter variations on the deep Atlantic [Si] and $\delta^{30}\text{Si}$ gradients (calculated as the difference between the deep high-latitude boxes; light blue shading) is shown in panel *b* (warm colours: $\Delta[\text{Si}]$ in μM ; cool colours: $\Delta\delta^{30}\text{Si}$ in ‰). PAZ: polar Antarctic zone; AZ: Antarctic zone. The light blue shaded region in panel *b* corresponds to observations ($\Delta[\text{Si}] \sim 108 \mu\text{M}$, $\Delta\delta^{30}\text{Si} \sim 0.5\text{‰}$).

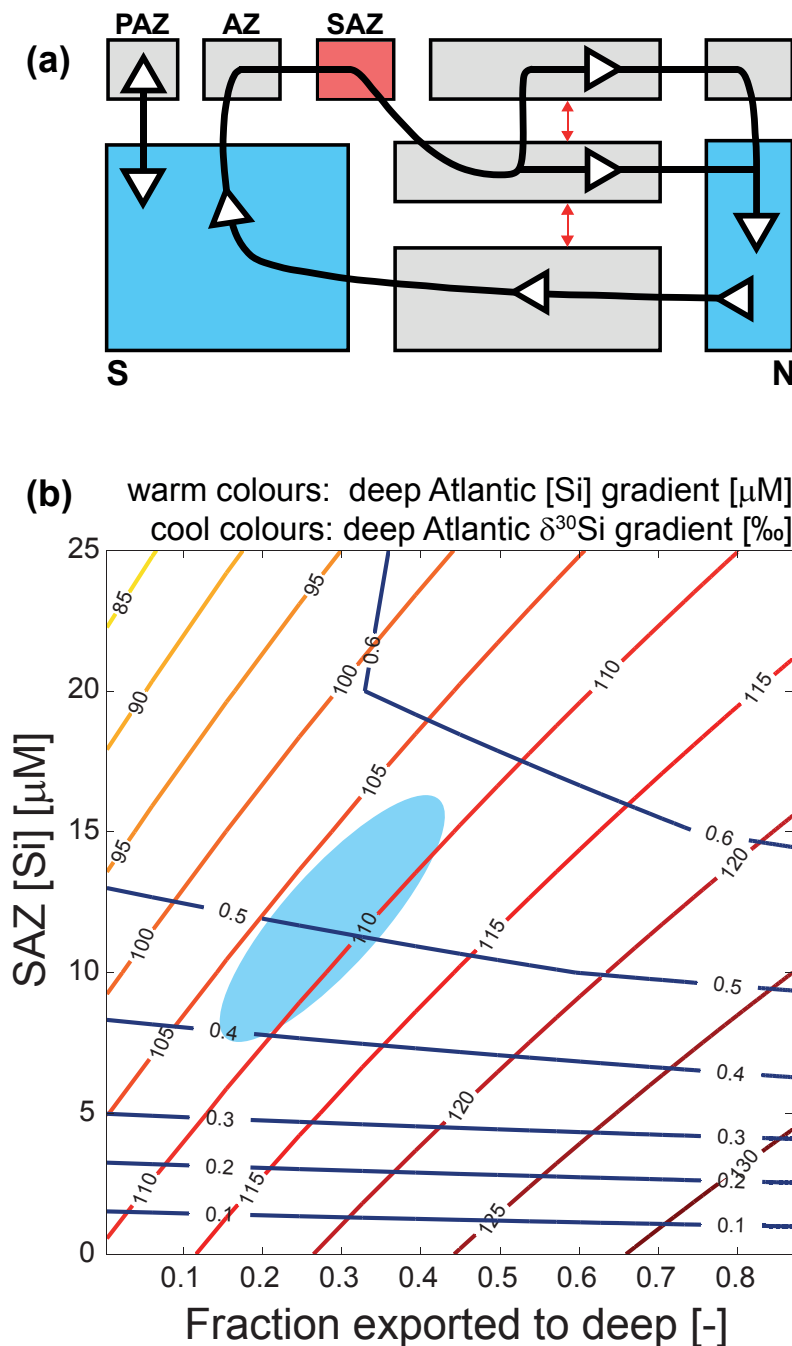


Fig. 3: (a) Theoretical model framework of Gnanadesikan (1999) and (b) northward meridional volume transport above the $\sigma_\theta = 27.4$ isopycnal in the suite of OGCMs used in this study, whose construction is based on the theory of Gnanadesikan (1999). In panel *a*, the depth D of the pycnocline (light blue shading) is maintained by the volume balance between flux T_n representing sinking of dense water in the North Atlantic, T_u representing low-latitude upwelling, and the balance between wind-driven northward Ekman transport T_w and eddy-induced southward transport T_e in the Southern Ocean.

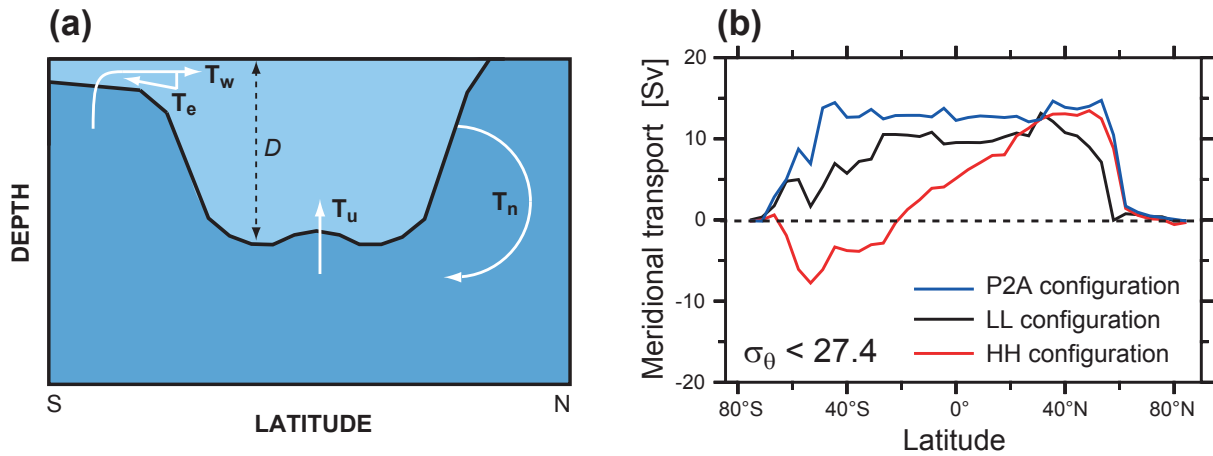


Fig. 4: Schematic meridional Atlantic section showing the tagging scheme employed to trace Si sources to the North Atlantic Ocean. Curved black lines represent potential density anomaly (σ_θ) surfaces labeled at their southern outcrop. Each coloured area represents a tagging region within which Si is assigned a source “identity”. Four sources of Si are traced: SAMW, AAIW, deep Southern Ocean (*DEEP*) and North Pacific (*NPAC*). The southern hemisphere tagging regions are circumpolar, whilst the NPAC tagging region is restricted to the North Pacific Ocean. The identity of Si tagged in any one region is destroyed when it enters another coloured tagging region, where it is assigned a new source identity. Within the grey area, tagged Si is cycled by biology and transported by the physical circulation analogously to the total Si pool.

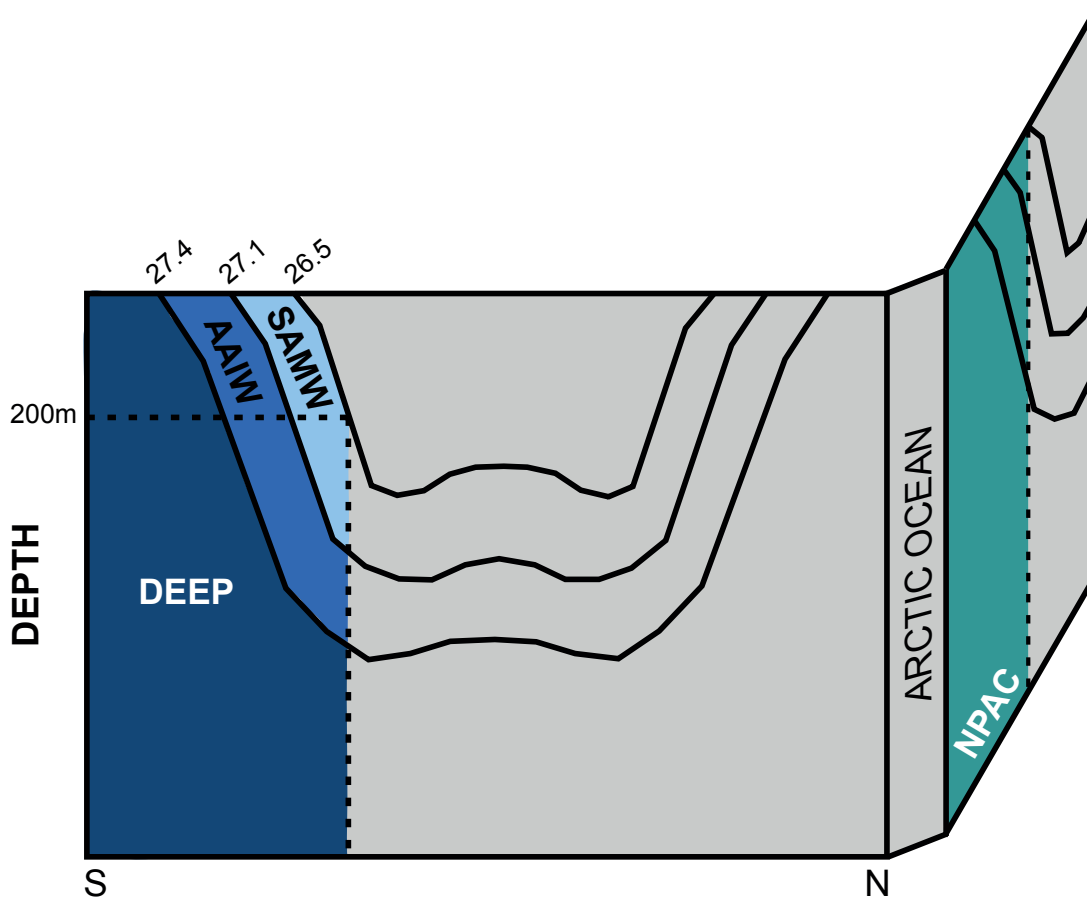


Fig. 5: Meridional sections showing the average Atlantic Si distribution in the uppermost 2400m in World Ocean Atlas 2009 (upper left) and the three model variants. Concentrations are averaged over the Atlantic basin, and over the Southern Ocean from 60°W to 30°E.

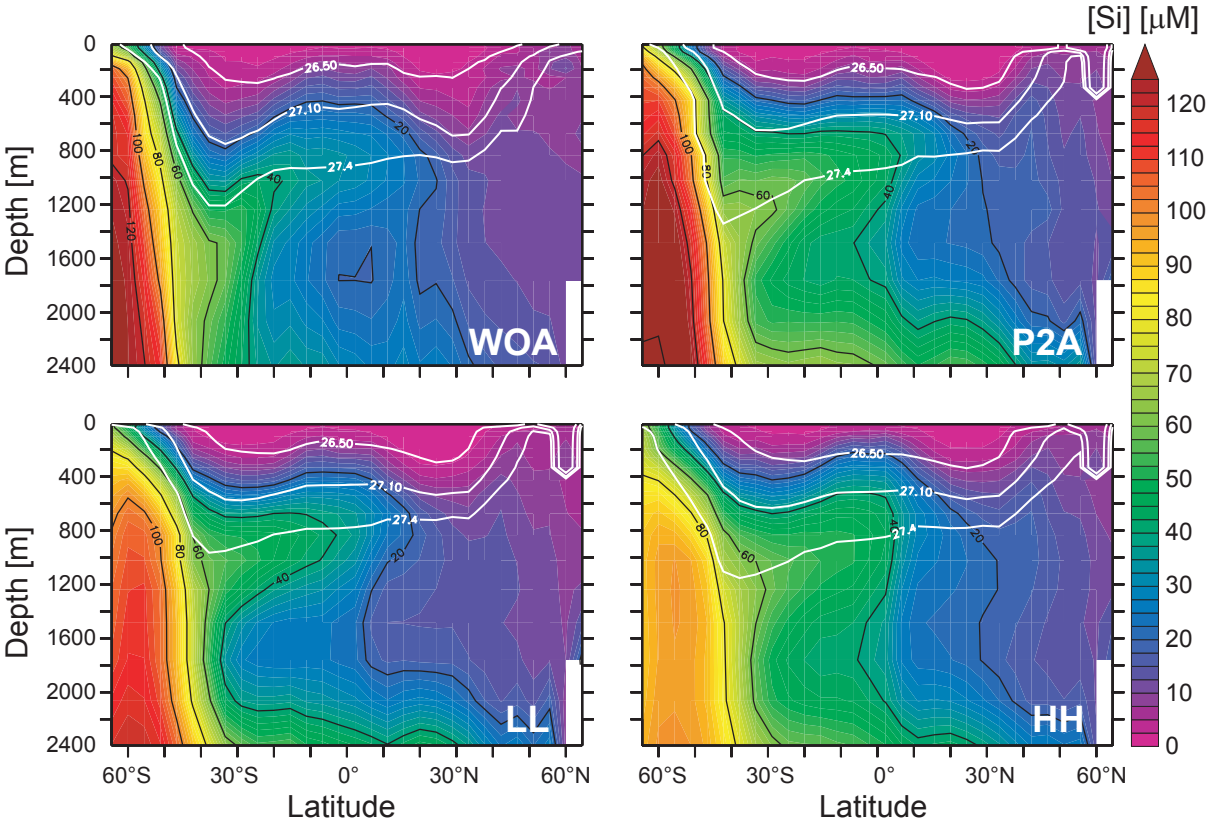


Fig. 6: Distribution of the contribution of each source region to the Si inventory of the thermocline ($\sigma_\theta < 26.8$) in the three model variants in the three model variants [mol Si/mol Si, unitless]. White shading indicates the absence of water lighter than $\sigma_\theta = 26.8$.

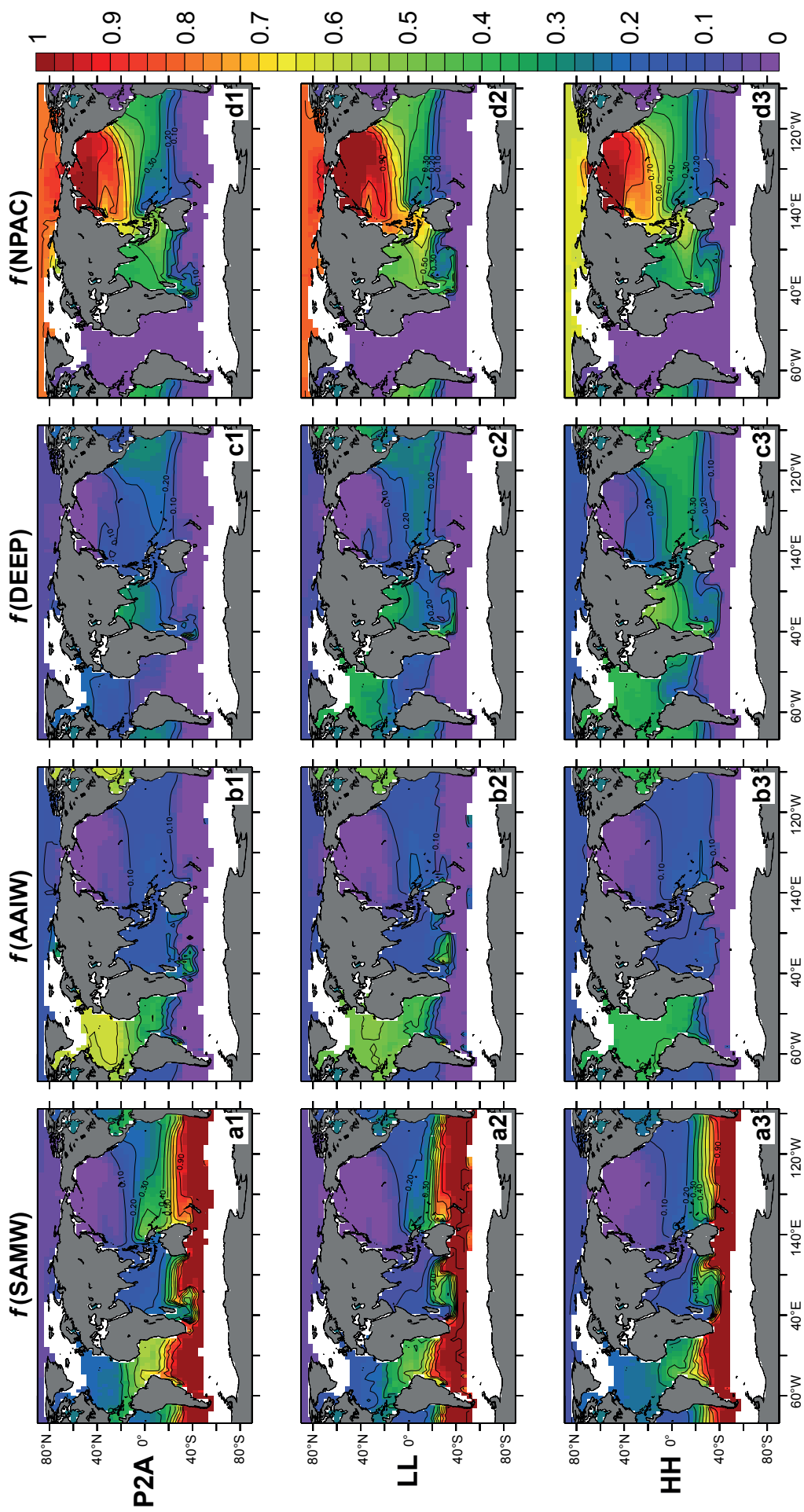


Fig. 7: Meridional section showing the Atlantic-average contribution of the four source regions to the Si inventory [mol Si/mol Si, unitless] in the uppermost 2400m of the three model variants. The three white contours correspond to the density horizons used to determine the tagging regions for SAMW- and AAIW-sourced Si (Fig. 4). Fractions are averaged over the Atlantic basin and over the Southern Ocean from 60°W to 30°E.

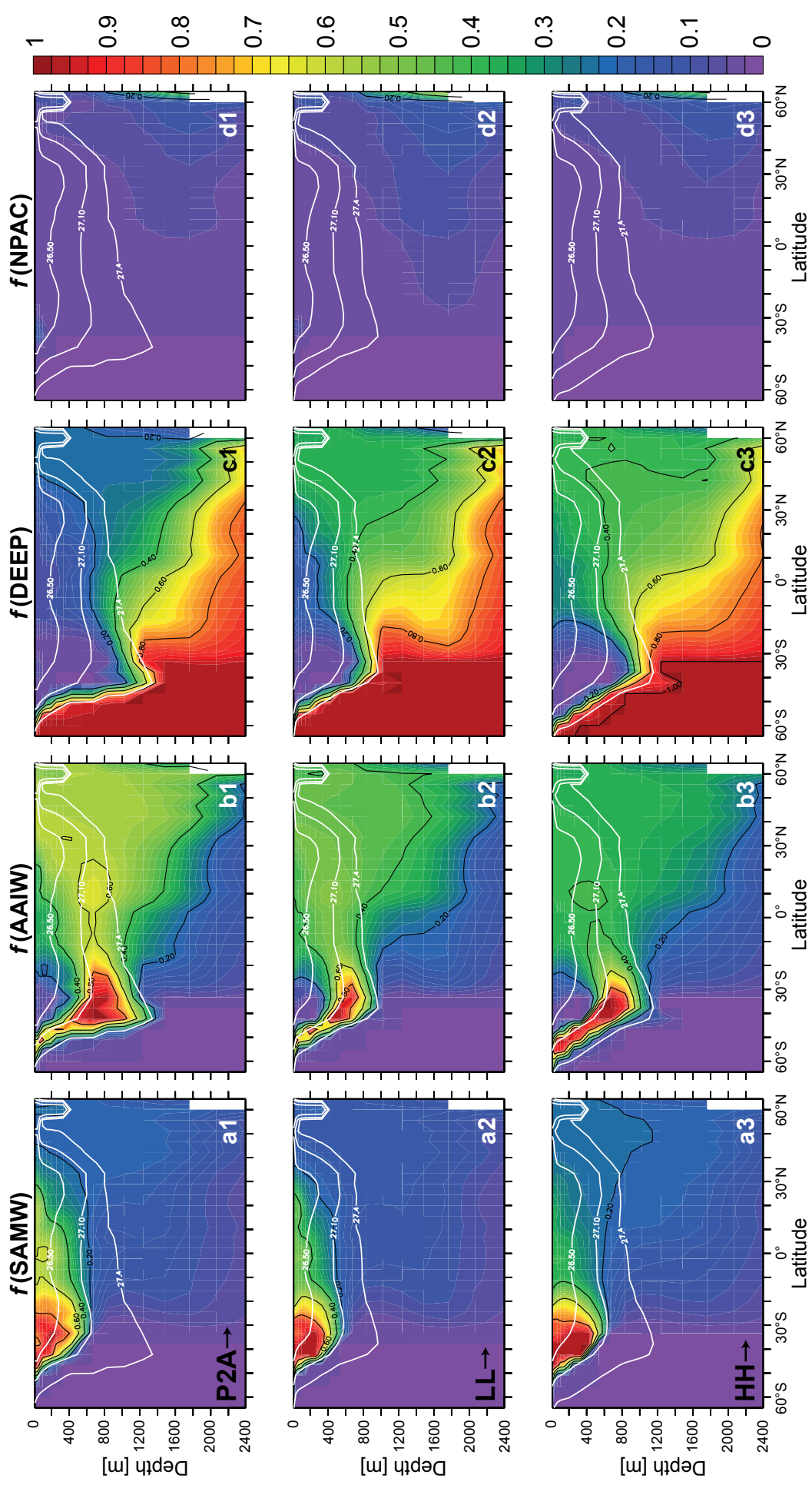


Fig. 8: Isotopic signatures and source composition of NADW in the North Atlantic Ocean. (a) Distribution of $\delta^{30}\text{Si}$ at $\sim 1700\text{m}$ water depth, illustrating the southward spreading of the high- $\delta^{30}\text{Si}$ signature of NADW as a deep western boundary current. The white dotted line at $\sim 43^\circ\text{N}$ in column *a* corresponds to the latitude of the depth sections in columns *b–d*, which show (b) the pre-industrial $\Delta^{14}\text{C}$ distribution (‰), (c) the $\delta^{30}\text{Si}$ distribution (‰), and (d) the fractional contribution of SAMW- and AAIW-derived Si to the Si inventory (mol Si/mol Si, unitless).

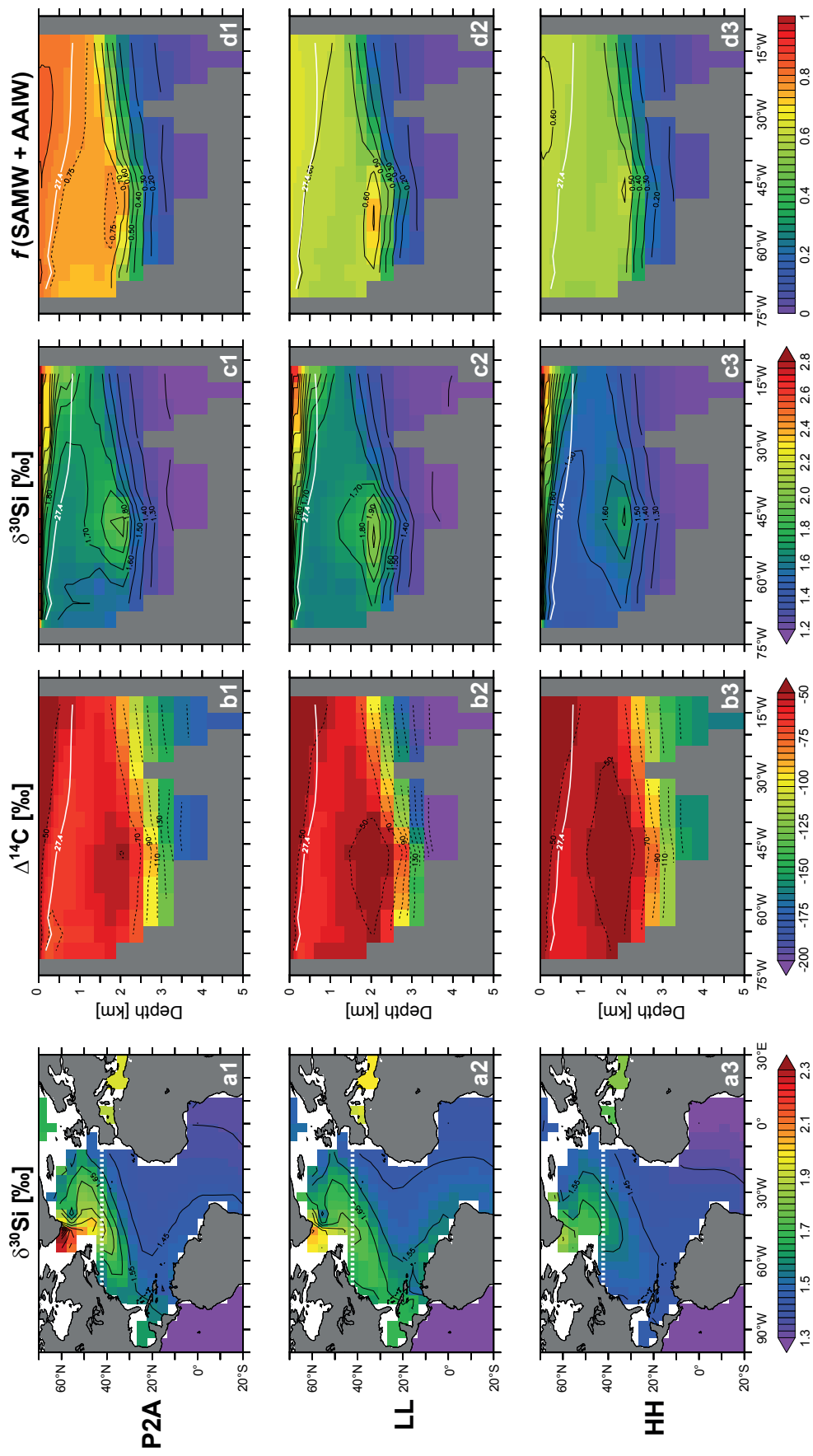


Fig. 9: Meridional sections at 25°W in the Atlantic Ocean from all three model variants, comparing (a) the simulated $\delta^{30}\text{Si}$ distribution with (b) the $\delta^{30}\text{Si}_{distal}$ distribution calculated using Eqn. 1, i.e. the $\delta^{30}\text{Si}$ distribution expected simply from propagation of source-region $\delta^{30}\text{Si}$ signatures. Panel *c* shows the difference between panels *a* and *b*. White solid lines are isopycnal surfaces used in the definition of *SAMW* and *AAIW* tagging regions (Fig. 4); the white dotted line marks 30°S, the northernmost extent of the *DEEP* tagging region. In panel *d*, a scatterplot directly compares the deep $\delta^{30}\text{Si}_{distal}$ distribution (> 1000 m) to the simulated $\delta^{30}\text{Si}$ distribution north of 30°S, illustrating both the clear correlation between the two fields as well as the muted dynamic range of $\delta^{30}\text{Si}_{distal}$.

